Benchmarking Signorini and exponential contact laws for an industrial train brake squeal application

G. Vermot des Roches [1,2], **O. Chiello** [3], **E. Balmes** [1,2], **X. Lorang** [4]
[1] SDTools
44 rue Vergniaud, 75013, Paris, France
e-mail: **vermot@sdtools.com**

[2] Arts et Metiers ParisTech
151 Boulevard de l'Hôpital, 75013, Paris, France

[3] IFSTTAR-LTE Laboratoire Transport et Environnement
25 avenue François Mitterrand, 69675, Bron CEDEX, France

[4] SNCF, Innovative and Research department
40 avenue des terroirs de France, 75611, Paris CEDEX 12, France

Abstract
Contact representation of structure interactions for finite element models is nowadays of great interest in the industry. Two contact modellig strategies exist in the literature, either based on a perfect contact with no interpenetration of structures at contact points, or based on functional laws releasing the contact constraint through pressure-penetration relationships. Both strategies require very different and rarely documented numerical implementations, making difficult any objective comparison. This paper presents a benchmark between ideal contact and a functional law of the exponential type applied to squeal simulations by complex mode analysis of an industrial railway brake.

1 Introduction

Increase of computational power and deployment of more and more efficient solvers dramatically increased simulation capabilities in the field of structural dynamics. Industrially, simulating interactions of multiple components in mechanical assemblies is thus of particular interest nowadays – this commonly requires contact and possibly friction models. The particular application of this paper concerns brake squeal for trains during station parking operations. Noise disturbances can raise issues in the vicinity of stations over a few kilometers, limiting train exploitations. The AcouFren project piloted by SNCF (the french railway company) thus aims at providing noise indicators at early brake design stages, through simulation.

Contact modelling strategies are widely documented in the literature, from which two trends are clearly found. The oldest representation is due to Signorini from the 30's, it *idealizes* a perfect contact between two ideally smooth bodies, and constrains the relative displacement of contact points. The second representation strategy is *functional* and authorizes a level of interpenetration between bodies. First measurements were performed in the 60's, from which Greenwood and Williamson [1] developed models where contact stiffness is function of the bodies interpenetration. State-of-the-art measurements as performed by Nogueira *et al.* [2] still show that this model can be relevant, mostly for hard surfaces. Direct ulstrasonic measurement of contact stiffnesses, can also be performed. Biwa *et al.* in [3] thus showed that contact stiffness is function of the contact pressure, mostly for low interfacial loading.

Physically speaking, contact between two bodies can be interpreted as the harmony between their respective stiffness and asperity compression, as illustrated in figure 1. When one material is much softer than the other, like for brake systems, local compression of asperities becomes non-negligible at the macroscopic scale, generating local interpenetration of the nominal surfaces (with sometimes plastic asperity deformation). It can then be relevant to identify a law $p(g)$ linking overclosure of nominal surfaces and contact pressure.

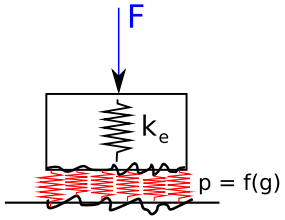

Figure 1: Representation of contact between two bodies, body stiffness and asperities

Numerically speaking, implementation of functional contact laws using continuous non linear functions of displacement is easier since classical non-linear algorithms can then be used. The ideal contact law does not feature any mechanical parameter to be identified, but its numerical implementation requires specific algorithms. Their convergence is often very sensitive and fine tuning of numerical parameters is needed. Besides, numerical convergence is often obtained regarding a tolerance, such that interpenetration could still occur in the results, with levels that are difficult to control.

Choosing a contact strategy is thus difficult and the general feeling is that these different contact models yield different results. The aim of this paper is to present an objective comparison of Signorini and exponential functional contact laws in application to an industrial train brake squeal simulation. Section 2 starts by presenting numerical implementation details of functional contact, based on the work of Vermot des Roches [4]. Signorini implementation is then presented, based on the work of Moirot [5]. Section 3 then aims at demonstrating that an equivalence between both contact laws is possible, and a functional law of the exponential type is proposed. Section 4 eventually presents a validation applied to industrial railway brakes.

2 Contact formulations for squeal simulations

Squeal simulations in the frequency domain is nowadays widely deployed in the industry, and is based on the *sliding perturbation* method. This was used by Moirot [5], Lorang [6] for train brake squeal applications, or by Vola *et al.* [7] to study rubber/glass instabilities in sliding steady states, and by Vermot des Roches in [4] for automotive brake squeal application. Contact formulations and adapted numerical schemes for squeal simulations are here presented.

2.1 Contact handling for finite element models

The representation of contact between two solids as formalized by Signorini is defined by a contact direction N along the outward normal at a contact point of one of the bodies (the chosen one, $S1$ is commonly called *master*, as contact forces will be evaluated on its surface). Figure 2 illustrates the contact configuration.

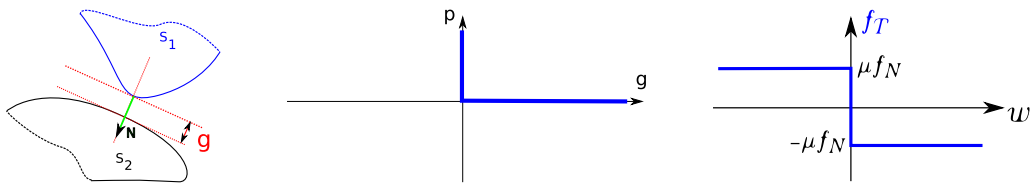

Figure 2: Contact normal (N) and gap (g) definition between solids, Signorini and Coulomb laws

The distance between the two bodies along the contact normal is called the *gap*, here noted g. The convention is that the gap is positive when contact is open, or not effective. When contact is closed, or effective, a contact pressure p exists between the bodies, applied at contact points, equal in amplitude on both solids. The contact law proposed by Signorini is illustrated in figure 2, it defines the condition of non-interpenetration as

$$\begin{cases} g \geq 0 \\ p \geq 0 \\ (g).(p) = 0 \end{cases} \tag{1}$$

Alternatively, functional contact laws define a pressure-gap relationship, they are sometimes exploited as numerical regularization means, or for physical reasons, using experimental characterization. Classical laws are illustrated in figure 3.

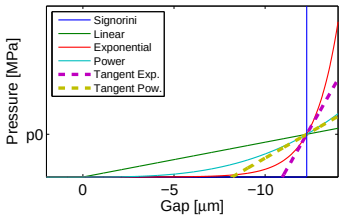

Figure 3: Classical contact laws, and their derivatives (for contact stiffness)

Numerically the gap is a linear observation of relative displacement between two surfaces along a normal, and can thus be written using an observation matrix $[C_{NOR}]$. Noting N the number of system DOF, and N_c the number of contact points, it is written with a possible gap offset $\{g_0\}$

$$\{g\}_{N_c \times 1} = [C_{NOR}]_{N_c \times N} \{q(u)\}_{N \times 1} - \{g_0\}_{N_c \times 1} \tag{2}$$

The force resulting from the gap-pressure relationship is then defined at each contact point as

$$\{\hat{q}\}^T \{f_N\} = \int_\Gamma \{\hat{u}(\hat{q})\}^T N p dS \simeq \sum_e \sum_j \{\hat{u}(\hat{q})\}^T \{N\} p(x_j, q) \omega_j^{(e)} J^{(e)}(x_j) \tag{3}$$

where f_N is the global contact force, p the contact pressure, $\hat{q}$ a virtual displacement, q the displacement, $x_j^{(e)}$ are the integration points of current element e, $J^{(e)}(x_j)$ the Jacobian of the shape transformation (surface associated to each integration point) and $\omega_j^{(e)}$ the weighting associated with the integration rule of element e. In practice contact forces can be recovered at nodes using the gap observation (2):

$$\{f_N\}_{N \times 1} = [C_{NOR}]^T_{N \times N_c} \left\{ \omega_j^{(e)} J^{(e)}(x_j)\, p(x_j, q) \right\}_{N_c \times 1} \tag{4}$$

The Coulomb law is expressed as

$$\begin{cases} \| \{f_T\} \| < \mu \| \{f_N\} \| \Leftrightarrow \{w\} = \{0\} \\ \| \{f_T\} \| = \mu \| \{f_N\} \| \Leftrightarrow \{f_T\} = \mu \| \{f_N\} \| \frac{\{w\}}{\|\{w\}\|} \end{cases} \tag{5}$$

where f_T is the friction force, μ the friction coefficient, and w the sliding velocity. Computation of the sliding velocity requires computation of differential velocities between slave and master surfaces in the plane orthogonal to the contact normal. A tangential displacement observation matrix $[C_{TAN}]$ can be used

$$\{w\}_{2N_c \times 1} = [C_{TAN}]_{2N_c \times N} \{\dot{q}\}_{N \times 1} \tag{6}$$

and friction forces can be recovered, from the local friction force f_{tj} by

$$\{f_T\}_{N \times 1} = [C_{TAN}]^T_{N \times 2N_c} \left\{ \omega_j^{(e)} J^{(e)}(x_j)\; f_{tj}(p(x_j, q)) \right\}_{2N_c \times 1} \tag{7}$$

For 3D solids, Moirot [5] noted that the sliding friction tangent state also features a damping term due to the possibility for the friction force to change its orientation in vibration. Physically, the higher the contact pressure, the more difficult the sliding direction variation. This is due to the priviledged sliding direction of the steady sliding state. A planar friction damping matrix $[C_{f2}]$ derived from the expression of friction forces thus appears, written

$$\delta f_T = [C_{f2}]\,\delta\dot{q} = [C_{TAN}]_2^T \left[\diagdown \frac{1}{\|w_i\|} \mu f_{Ni} \diagdown \right] [C_{TAN}]_2\,\delta\dot{q} \tag{8}$$

2.2 Functional contact

For functional contact formulations, classical non-linear methods can be applied, since contact-friction forces only depend on the system state. Given the system elastic stiffness $[K_{el}]$, and a displacement vector $\{q\}$, the system must verify

$$[K_{el}]\,\{q\} = \{f_{ext}\} + \{f_{NL}(q)\} \tag{9}$$

where the non linear force vector can be decomposed as $\{f_{NL}(q)\} = \{f_N(q)\} + \{f_T(q)\}$, with $\{f_N\}$ the contact forces and $\{f_T\}$ the friction forces.

2.2.1 Functional contact statics

The most classical method to resolve regular non linear statics is to use the Newton method, presented in figure 4. Stakes in Newton resolution algorithms are mostly on the numerical side. Although mathematical convergence is obtained theoretically when the system is *regular enough*, *hard laws* like contact implementations are challenging.

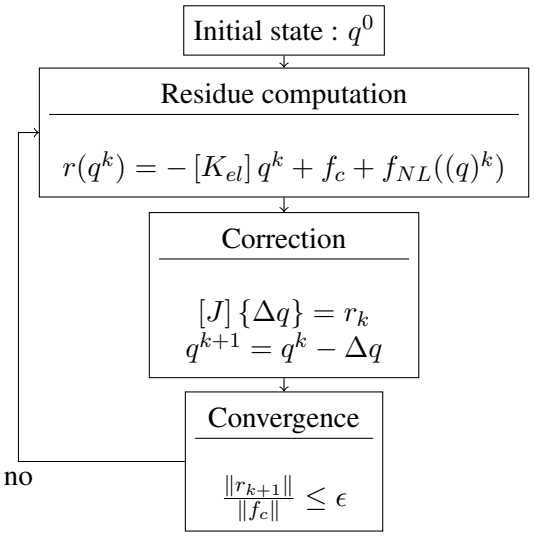

Figure 4: Implementation of a static Newton resolution scheme

The system Jacobian $[J]$ derived from (9) can be written

$$[J] = [K_{el}] + [K_c(g)] \tag{10}$$

Considering a steady sliding state, the tangent friction perturbation is null. Noting $\omega_j J(x_i)$ is the surface associated to each contact point. the tangent contact state defining $[K_c(g)]$ writes

$$\frac{\partial f_N(q+\delta q)}{\partial \delta q} = [C_{NOR}]^T \left[\diagdown \omega_j J(x_i) \diagdown \right] \left[\frac{\partial p(q+\delta q)}{\partial \delta q} \right] [C_{NOR}] = [C_{NOR}]^T \left[\diagdown k_{ci}(q) \diagdown \right] [C_{NOR}] \tag{11}$$

For hard laws tangent state variation can be very brutal, which is a drawback of such algorithms. Indeed, when contact opening occurs in a loaded area at iteration k, tangent contact state becomes locally null, and correction can become very large (with possibly contact overclosures). Divergence can then quickly occur as the non-linear forces returned to the large overclosures can overcome numerical conditioning and machine capabilities (infinite forces).

A full set of adaptations can be applied to the original Newton scheme, yielding numerous variations of quasi-Newton methods. For hard contact, cut-backs on corrections based on the mechanical residue norm, and controlled release on the contact part of the Jacobian for opening points are usually working and have been used here. Implementation details is key here to performance, but are outside this paper scope.

2.2.2 Functional contact sliding perturbation formulation

Functional contact formulations are defined as function of the gap, such that a tangent state can be derived for each contact point by deriving the gap/pressure relation, illustrated in figure 3. A key aspect to note is that for a similar contact pressure level, different functional contact laws can yield very different contact stiffnesses. Contact law calibration in statics and dynamics can then be uncorrelated.

Definition of tangent contact stiffness has been defined in (11). Defining tangent friction states is less direct as it couples normal and tangential directions, which is typically non-symmetric. Friction expression (5) indeed shows that a variation of contact force has a direct effect on friction force, whereas friction force variation may occur without effect on contact force.

For sliding states, friction force is explicitly defined and only depends on contact force at the same point. The tangent friction stiffness is then the tangent contact stiffness (11) scaled by the friction coefficient μ, and transfers normal displacement to planar force. Since planar displacements are free for a fixed contact state, this effect is not considered for real mode computation. The tangent sliding friction coupling stiffness K_{nlf}^{slide} is thus defined as

$$K_{nlf}^{slide} = \begin{cases} 0 & \text{for real mode computation} \\ [C_{TAN}]^T \left[\backslash \mu k_{ci}(q) \backslash \right] [C_{NOR}] & \text{for complex mode computation} \end{cases} \tag{12}$$

2.3 Signorini contact

Ideal contact verifying the exact Signorini condition (9) is non regular, hence the common name of *non-smooth dynamics*. $\{f_{NL}(q)\}$ has no specific link to the displacement, and the pair $(\{q\}, \{f_{NL}\})$ has to be directly solved.

2.3.1 Signorini statics

Resolution strategies are usually based on Lagrange resolutions. The non-symmetric nature of friction requires a methodology refinement, using *Augmented-Lagrange* methods. De Saxcé and Feng developed the *bipotential* method [8]. Alart *et al.* presented a generalization of the Newton method adapted to Lagrange formulations introducing Gauss–Siedel like algorithms [9].

The resolution chosen here was developped by Moirot [5]. It is based on the status assumption of each contact points (open/closed gap). Closed contact points generate a displacement constraint under which resolution is linear. Noting with superscript $^{(e)}$ the observation restricted to conctact points in effectively closed contact, one resolves the problem in an orthogonal subspace $T^{(e)}$ defined as

$$\{q\} = \left[T^{(e)}\right] \{q_e\} \,/\, [C_{NOR}]^{(e)} \{q_e\} = 0 \tag{13}$$

Equation (9) can thus be written

$$\left[T^{(e)}\right]^T [K_{el}] \left[T^{(e)}\right] \{q_e\} = \left[T^{(e)}\right]^T (\{f_{ext}\} + \{f_N\} + \{f_T\}) \tag{14}$$

Since contact constraints are verified, contact forces are known

$$\{f_N\} = [C_{NOR}]^{(e)} ([K_{el}] \{q\} - \{f_{ext}\}) \tag{15}$$

and are null in $T^{(e)}$. Sliding friction forces (5) can thus be written

$$\{f_T\} = \mu [C_{TAN}]^T [C_{NOR}] ([K_{el}] \{q\} - \{f_{ext}\}) \tag{16}$$

which is a little simplified in $T^{(e)}$. Equation (14) becomes

$$\left[T^{(e)}\right]^T \left([\mathcal{I}] - \mu [C_{TAN}]^T [C_{NOR}]\right) [K_{el}] \left[T^{(e)}\right] \{q\} = \left[T^{(e)}\right]^T \left([\mathcal{I}] - \mu [C_{TAN}]^T [C_{NOR}]\right) \{f_{ext}\} \tag{17}$$

It must be noted that the factor $\left([\mathcal{I}] - \mu [C_{TAN}]^T [C_{NOR}]\right)$ is not symmetric. Direct resolution can then be challenging for large problems, like the million-DOF system presented in section 4. Use of the latest PARDISO librairies [10], implemented in SDT [11] was here required.

Contact status must be predicted, and can be updated depending on the result of (17). This is formalized by considering the group of contact nodes considered in effective contact in (17) and verifying Signorini (1). This group noted $\mathcal{C}_k$ is defined by

$$\begin{cases} \forall x_j \in \mathcal{C}_k, f_N(x_j) \geq 0 \\ \text{and} \\ \forall x_j \notin \mathcal{C}_k, g(x_j) \geq 0 \end{cases} \tag{18}$$

At each iteration, contact points violating Signorini conditions are classed in group $\mathcal{D}_k$ such that

$$\begin{cases} x_j \in \mathcal{C}_k, f_N(x_j) < 0 \\ \text{or} \\ x_j \notin \mathcal{C}_k, g(x_j) < 0 \end{cases} \tag{19}$$

Status updating allows forming a new $[C_{NOR}]^{(e)}$ and consists in switching the status of points in $\mathcal{D}_k$,

$$\mathcal{C}_{k+1} = (\mathcal{C}_k - \mathcal{C}_k \cap \mathcal{D}_k) \cup (\mathcal{D}_k - \mathcal{D}_k \cap \mathcal{C}_k) \tag{20}$$

Iterative status correction can be resolved by an Uzawa algorithm, presented in figure 5. This method convergence has been proved without friction and by switching contact statuses one by one. Its performance is however very satisfying in this paper application, with very little iterations even for complex systems and high friction coefficients.

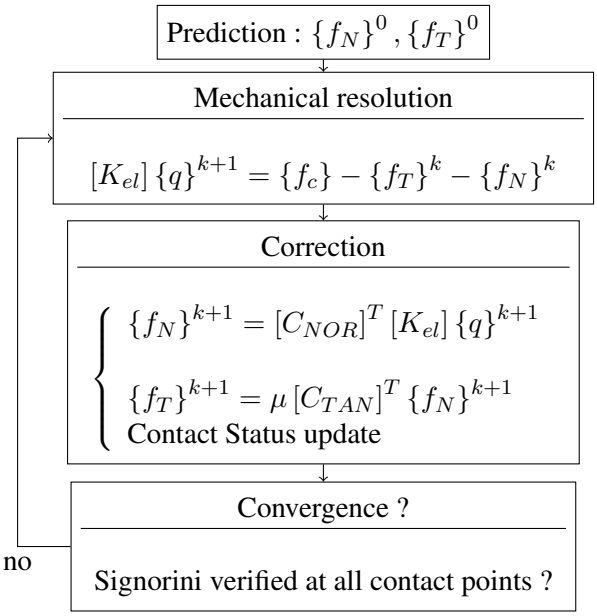

Figure 5: Implementation of an Uzawa resolution algorithm for the Signorini-Coulomb contact-friction laws

2.3.2 Signorini modal analysis

Following the exact contact condition of Signorini, the system tangent state only depends on the contact surface, materialised by $\mathcal{C}_\infty$, as presented in 2.3.1. The mechanical problem is here formulated as

$$\begin{cases} \left(\lambda^2 [M_{el}] + \lambda ([C_{el}] + [C_{f2}]) + [K_{el}]\right) \{q\} = \{f_{NL}\} \\ [C_{NOR}]^{(e)} \{q\} = 0 \end{cases} \tag{21}$$

Like for static resolution, projection in the subspace orthogonal to the contact constraints $T^{(e)}$ yields

$$\left(\lambda^2 \left[M_\mu^{(e)}\right] + \lambda \left(\left[C_\mu^{(e)}\right] + [C_{f2}]\right) + \left[K_\mu^{(e)}\right]\right) \{q_e\} = 0 \tag{22}$$

where matrices $\left[X_\mu^{(e)}\right]$ are the so-called *sliding matrices*, defined as

$$\left[X_\mu^{(e)}\right] = \left(\mathcal{I} - [C_{TAN}]^T [C_{NOR}]\right) \left[T^{(e)}\right]^T [X_{el}] \left[T^{(e)}\right] \tag{23}$$

3 Definition of an exponential contact law

The two contact implementation methods presented in section 2 are numerically very different, and require different resolution algorithms. The concept of figure 1 is here exploited to show that functional laws can be calibrated to provide equivalent results to the ideal law. This section thus aims at presenting a relevant type of functional contact law and its numerical calibration.

3.1 The clamped/sliding block

The railway industry pads can be of different shapes and materials, a sample one named G35 is presented in figure 6. A friction block (made of friction material) is extracted for this section illustration. The block is here solidar to a metallic ring making the link to the backplate. The friction material has a non-negligible loss-factor, modelled by a material Rayleigh damping (easy compatibility for transient simulations).

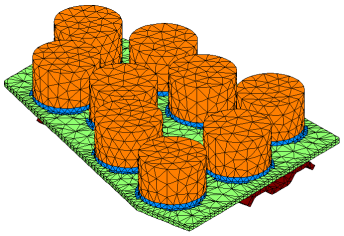

Figure 6: A sample railway braking pad. The friction blocks in orange are linked to the backplate in green, using rings in blue. A dovetail joint (in red) fixes the pad in the brake rig.

When computing steady sliding states, and sliding perturbations, the friction blocks effective contact area is supposed to be fully sliding (although some contacts can be opened). A sample demonstration of the blocks behavior is thus to consider them in clamped/sliding condition. Ideal contact condition is materialized in this case by clamping normal displacements of the friction block bottom side. Figure 7 shows some modes associated to the pad block in such conditions.

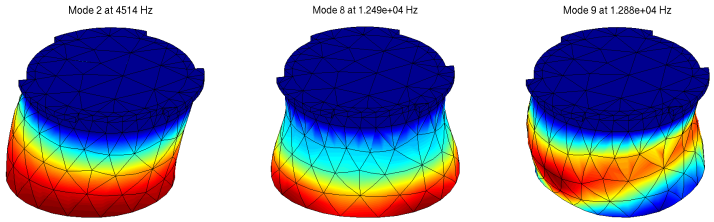

Figure 7: Sample block modes in clamped/sliding conditions with ideal contact for the G35 ring fitted block.

To demonstrate the effect of contact stiffness (possibly derived from a functional contact law), normal spring elements of parametered stiffness are added to the blocks bottoms instead of clamping. The previous case would then correspond to a spring with infinite stiffness.

Figure 8 presents complex mode frequency and damping results of the clamped sliding block as function of contact stiffness, an *S-shaped* frequency evolution can be observed. Saturation occurs around $10^4 MPa$, after which frequencies are equivalent to an ideal contact implementation.

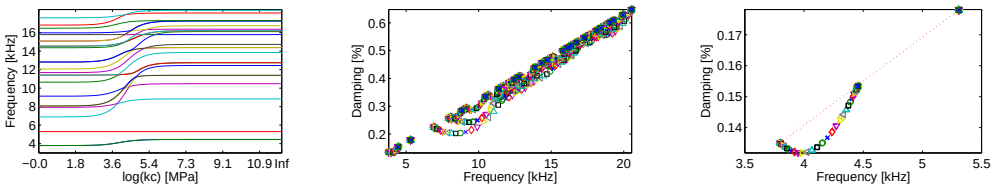

Figure 8: Frequency (left) and damping (middle) evolution as function of the contact stiffness applied to the lining block of the G35 pad. Right: zoom in on the first modes.

Mode damping evolution as function of contact stiffness can be observed in figure 8. Damping rates increase with frequency as a consequence of the stiffness proportionality coefficient used to form the material Rayleigh damping matrix.

An interesting behavior can here be seen when contact stiffness is located of the frequency curve inflection area, seen in figure 8. For low contact stiffnesses, ground coupling is small and the friction block behaves as free, that-is-to-say the whole strain energy is located in the block. Damping ratio of the clamped/sliding block is thus linked to the damping ratio of the block itself. The same observation can be done for high contact stiffnesses, when coupling is strong and the friction block behaves as clamped. The expected damping ratio increase is obtained regarding the frequency increase, materialized bythe dotted line in figure 8.

In the curve inflection area, a non negligible strain energy is located in the coupling springs, so that a non negligible part of the total system strain energy is outside the friction block. The damping ratio thus varies less than the linear evolution expected, and can even decrease when coupling becomes non negligible while still being low. This observation is very general regarding impact of components strain energy distribution in damping of assemblies. More detailed illustrations of this effect can be found in [12].

3.2 Exponential contact law definition

There exists a large variety of functional contact laws that could be calibrated, the exponential type only is retained here. This choice is more fonded on the expected transient behavior, where contact opening transitions and penetration saturation effects also need to be properly approached for a potentially large range of pressures. Numerical results obtained in [4] with such law were satisfying.

Given $\{g\}$ the gap vector (the opposite of the overclosure vector), obtained from an observation of the relative displacement of both surfaces along the local contact normal, pressure $\{p\}$ is defined as

$$\{p\} = p_0 e^{-\lambda\{g\}} \tag{24}$$

The exponential law has two parameters p_0 and λ, whose effect on contact behavior is illustrated in figure 9. To interpret these curves, values have to be observed as function of a reference force level, conceptually named F. Horizontal intersections are thus iso-values regarding system loading outside the contact area.

Parameter p_0 only drives the curve offset, thus the level of gap obtained for a given force. Identification of such parameter can be obtained if measurements of surface rougthness are accessible, providing acceptable values of interpenetrations. Coefficients are only numerically calibrated in this paper so p_0 can be arbitrarily set. Choosing a p_0 such that significant contact pressures is obtained for closed (or negative) gaps, simplifies implementation and allows easier physical interpretations.

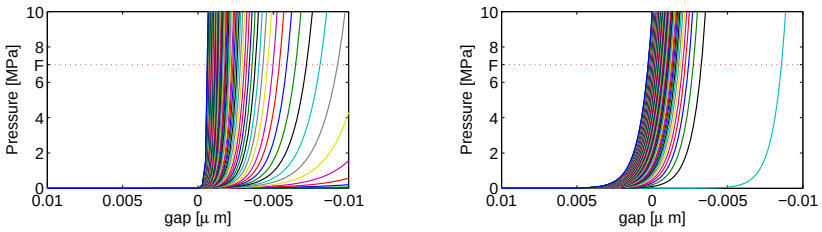

(a) $p_0 = 10^4, \lambda \in (10^2; 10^{10}) m^{-1}$ (b) $\lambda = 1.3.10^9, p_0 \in (10^2; 10^7) Pa$

Figure 9: Exponential contact law evolution as function of its parameters

Parameter λ impacts contact stiffness at a given force level, the higher, the stiffer. This parameter itself can thus be updated to choose a contact stiffness that complies with the fact that the block frequencies in clamped/sliding conditions are converged towards the behavior in perfect contact. Looking at the diagrams of figure 8, target contact stiffnesses values can be pin-pointed in figure 10.

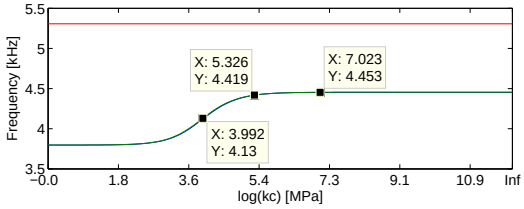

(a) Stiffness identification

Target stiffness [MPa]	$\lambda[mm^{-1}]$
10^7	$4.28\ 10^7$
$10^{5.3}$	$9.64\ 10^5$
10^4	$4.83\ 10^4$

(b) Table 3.2 : Correspondances

Figure 10: Identification of target contact stiffnesses of the clamped/sliding block, and identified λ

For calibration, the level of contact pressure generated by the system must be evaluated, either by using a status implementation or by choosing a linear contact law for a preliminary computation, or by exploiting the system command (the case here). Noting p_1 the obtained reference, contact pressure expression and the contact stiffness $k_c(g)$ (first order derivative of contact pressure) yield

$$\begin{cases} p_1 = p_0 e^{\lambda g} \\ k_c(g) = \lambda p_0 e^{-\lambda g} \end{cases} \tag{25}$$

The product λg can be substituted in the first equation of (25) such that

$$\lambda = \frac{k_c(g)}{p_1} \tag{26}$$

Choosing a target value of $10^7 MPa$ in figure 10, and knowing that the contact force command on the TGV brake system is here of $5kN$ over a surface of 21.4 $10^3 mm^2$, one obtains $\lambda = 4.28\ 10^7 mm^{-1}$. Higher values could also be used for security margin regarding system variability. It must however be kept in mind that values with too high stiffness may alter numerical conditioning of the stability problem.

For comparison means, a converged value $kc = 10^{5.3} MPa$ at the limit, and a non converged value $kc = 10^4 MPa$ will also be tested. Correspondances between λ and target stiffnesses are reported in table 3.2.

4 Application to industrial railway brakes

The french high speed train, TGV, features 4 disc brake systems on each axle, as presented in figure 11. A single brake system is here modelled by finite elements on which subassemblies (the disc, rig and pads) have been updated. The full model is free-meshed using second order ten nodes tetraedrons, yielding between 500,000 and 1,000,000 DOF depending on the fitted pad model.

The mesh is kinematically positioned depending on the pad thickness to have zero gap at the origin. Disc sections underlying the pads are remeshed to obtain compatible contact interfaces. Braking force is applied by an actuator at the system rear, which translates the pad holder towards the disc. The translation is kinematically realized by the rotations of levers and rods, constituting the brake rig.

(a) TGV

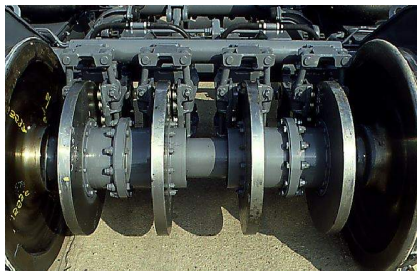

(b) 4 TGV discs on a TGV axle

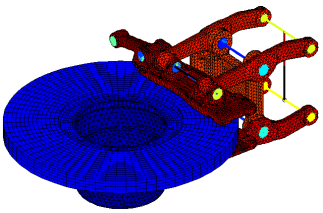

(c) TGV brake FEM

Figure 11: The TGV brake system

This paper application focuses on complex mode evaluation for station parking operations. Comparisons between calibrated exponential laws, defined in section 3.2 and the ideal contact implemenation are presented for steady state solutions in section 4.1 and complex modes in section 4.2.

4.1 Steady sliding simulations

A contact force command of $5kN$ is applied by the actuator. Figure 12 presents global steady sliding solution with ideal contact implementation. Levels of displacement and contact force resultants are presented. Largest

displacements are seen by the lever with values aournd $140\mu m$. Contact force distribution greatly varies over the contact surface. Friction blocks of the front end are the most loaded, unloading of the trailing end seems complicated and is function of the pad holder fixations.

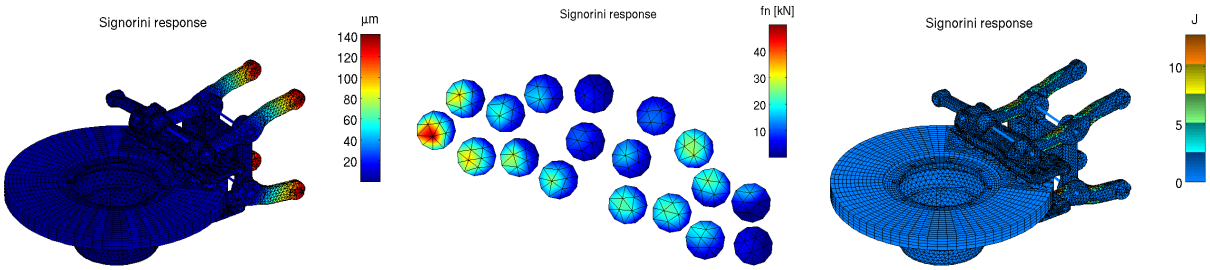

Figure 12: Steady sliding state absolute displacement of a TGV brake using Signorini contact implementation, contact resultant at contact nodes of the disc top side, and strain energy density distribution

Static results are compared between Signorini contact and the family of exponential contact laws defined in table 3.2. In the following, *contact nodes* define nodes of the mesh in the contact area, while *Gauss contact points* define the Gauss contact integration points used for functional contact implementation.

Figure 13 presents contact results in terms of pressure and gaps. Points with opened gaps at contact nodes are presented in figure 13a. It can be seen that no global difference rises for these displacements. Although contact pressure from an exponential law is strictly positive, exponential decay as function of opening is sufficient not to alter behavior of unloaded contact points.

Figure 13b presents gap results for closed contact. Great differences can here be observed, the softer the law, the deeper the penetration. Penetration levels seem reasonable regarding global displacements for converged λ values only.

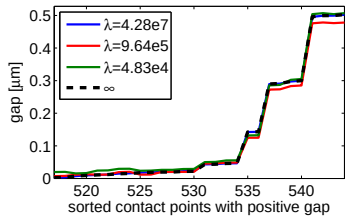

(a) Gaps at open points

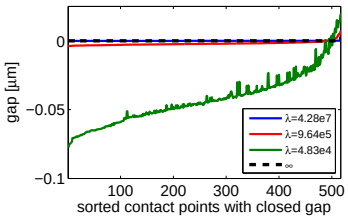

(b) Gaps at closed points

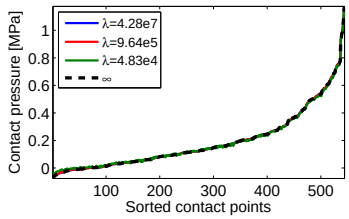

(c) Contact pressure at nodes

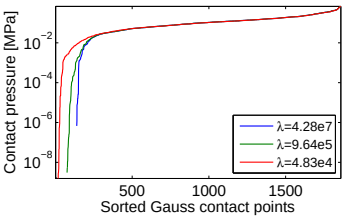

(d) Contact pressures at Gauss points

Figure 13: Comparative gaps and contact pressures between Signorini and exponential laws resuls.

Figure 13c presents contact pressure at contact nodes. Contact pressures at the interface are here *a posteriori* computed from displacements to allow comparison between implementations, using a nodal resultant to nodal pressure operator. Opened contact points will thus show negative pressures at the interface, which would correspond to depressions on a membrane. Such observation shows that pressure levels seen by the structure outside the interface are very similar. Forces transmitted by the interface are naturally recovered in all cases, which is physically natural.

Global results in figure 13c can be put into perspective with the local results of figure 13d. Contact pressures are here plotted at the Gauss contact points for the functional laws only. Clear differences occur for low pressure areas, with a convergence pattern as function of λ. Such fluctuations for very low pressures are however not percieved by the structure.

Figure 14 presents absolute differences in displacement between the Signorini response and functional contact laws. It can be seen that for all cases, maximum differences scale in nanometers, a thousand times smaller than displacement scale.

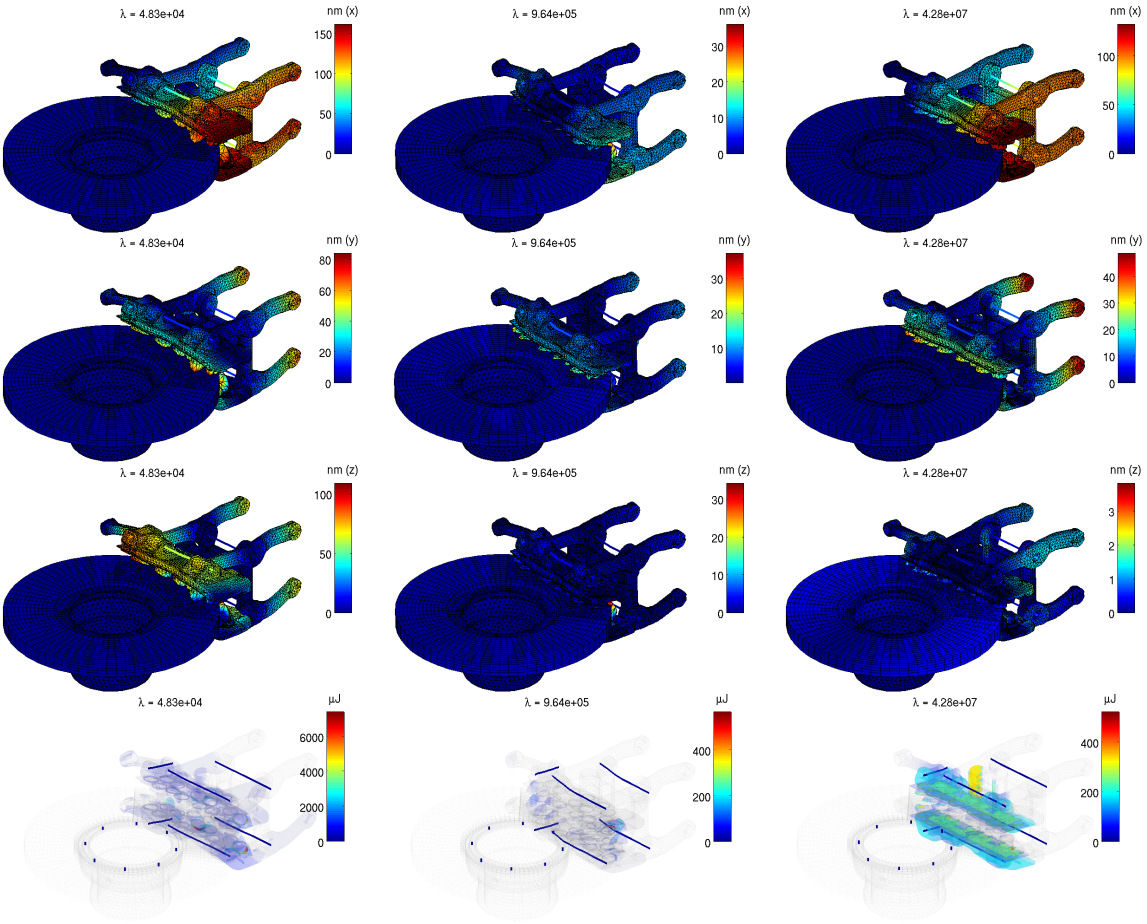

Figure 14: Absolute displacement differences in nanometers between Signorini and functional static results, from top to bottom along the x, y and z axis, from left to right in increasing λ. Strain enrgy densities of differential displacements are presented for elements with highest levels only

Axis references are provided in figure 11. Convergence in the z axis is direclty linked to gap observations of figure 13b, and is clearly established as function of λ. Displacements in the x, y plane are linked to the rig deformation, depending on the pad holder displacement. Larger differences can here occur, with very limited strain energy errors for converged cases. Athough static displacement seems better for the middle law, contact stiffness distribution is not as good, as discussed in section 4.2.

4.2 Sliding perturbation results

Complex modes are here directly computed based on the formulations presented in section 2. Stability diagrams are presented in figure 15 for 500 modes, providing a frequency bandwidth of $0 - 10kHz$. The global stability diagram of figure 15b shows the effect of material Rayleigh damping, with very large damping ratios on the first modes (mass factor) and an average damping ratio linear increase with frequency (stiffness factor).

The first four most unstable modes are plotted in figure 15a and 15c. Modes 27 and 69 are pad/disc coupling modes, with effective displacement of the pad holder. Modes 81 and 59 are *planar* modes, instability coming from friction block modes (possibly coupled with in-plane disc modes). No unstable modes are found for high frequencies in this configuration – Rayleigh damping coefficient stills needed experimental fitting in this study's model.

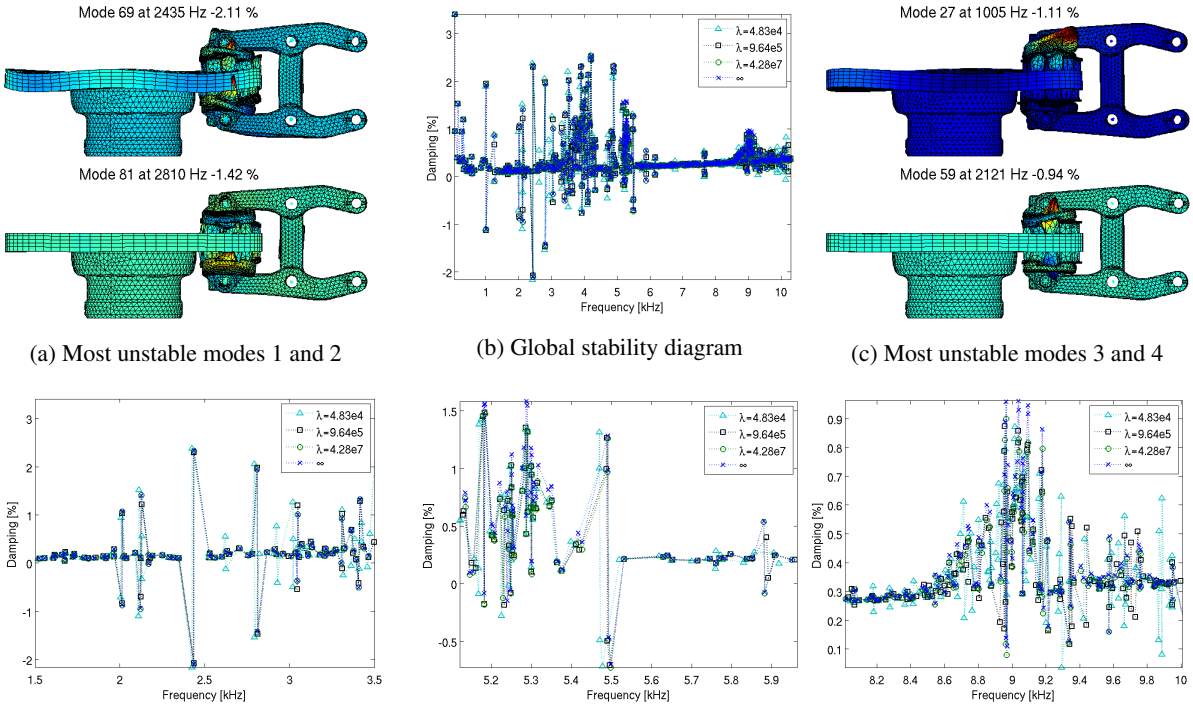

(a) Most unstable modes 1 and 2

(b) Global stability diagram

(c) Most unstable modes 3 and 4

(d) Zoom in on $2kHz$

(e) Zoom in on $5.5kHz$

(f) Zoom in on $9kHz$

Figure 15: Stability diagrams of Signorini solutions and functional law solutions. Most unstable TGV modes

One of the main interest of functional contact laws is the representaton of a contact stiffness distribution depending on contact pressure, whose variation can be non negligible for low pressures [3]. This is impossible with Signorini contact, where this pattern can only be assessed by evaluating contact opening thresholds as function of complex mode amplitudes.

Globally, stability diagrams fit relatively well for all exponential calibrations. Larger differences are obvious for the soft value, highlighting a convergence as function of λ. Zooms in are provided in figures 15d, 15e and 15f. Structure modes (with clear displacement of the brake rig) are in the $2kHz$ range, and show correct fittings, although the soft law presents some peculiarities.

Modes in the $5.5kHz$ and $9kHz$ ranges mostly feature friction block modes. Slight differences between *converged* λ values and Signorini are mostly due to contact stiffness variation of low contact pressure areas. A very good stability diagram fitting is here only obtained for the hardest value of λ.

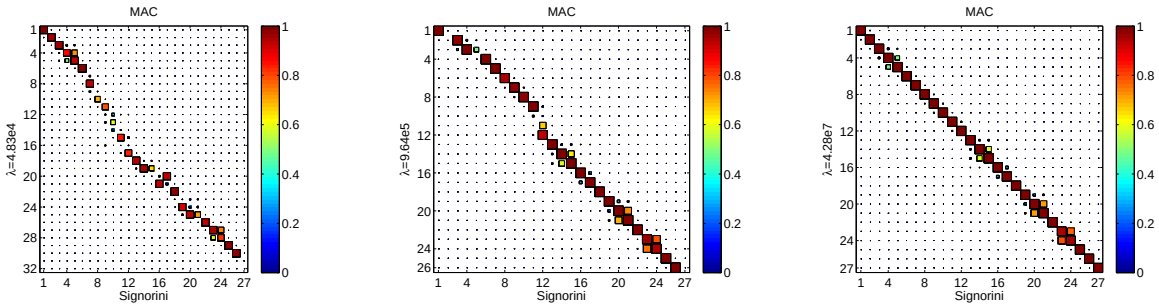

(a) $\lambda = 4.83.10^4$ (b) $\lambda = 9.64.10^5$ (c) $\lambda = 4.28.10^7$

Figure 16: Unstable modes ($\zeta \leq -10^{-3}\%$) MAC between Signorini and exponential laws solutions

Comparison between unstable modes with MAC is eventually presented in figure 16. Due to the large amount of modes computed and model size, each mode basis weights over 3 GBytes, making direct comparisons difficult. Unstable modes are of higher interest due to their propensity to generate squeal, hence the choice to compare only these shapes, with a detection threshold set under a damping ratio of $-10^{-3}\%$.

Convergence as function of λ is well observed regarding the number of detected unstable modes and their shape correlation, figure 16c displays a squared matrix with unitary diagonal. More unstable modes with no representation in the Signorini results are found for the two softest λ values.

5 Conclusion

Simulation of structure-structure interaction is now at stakes for industries, requirering performant implementation of relevant contact models. For the two dominant contact modelling strategies found in the literature, efficient implementation is available, but lacks benchmarking.

Physically, transmission of contact forces between structures should naturally show correct contact pressures independently from the contact law. Ideal laws avoids identification of physical parameters, but also lacks representation of contact stiffness variation as function of contact pressure. Functional laws require identification from difficult to realize experimentation. It was however shown that numerical calibration is sufficient and can be performed by considering the system apparent stiffness seen at interfaces.

The application presented in this paper, concerning squeal simulation of industrial brake squeal with complex mode analysis in the sliding perturbation framework, allowed benchmarking ideal and exponential contact. The advantage of the exponential law over other types is the quick decay of contact forces for opened gaps, while keeping relevant saturation patterns. Satisfying results are thus obtained for frequency and transient simulations. The objective comparison obtained confirmed that pressures transmitted between structures are independent from the contact strategy.

Implementation choices can thus be performed considering experimental capability and performance, with an insurance of results convergence. A clear perspective is a benchmark extension to transient simulations, available with methods such as presented in [4]. Such simulations are there so intensive that choice can only be directed by numerical performance.

References

[1] J. A. Greenwood and J. B. P. Williamson, “Contact of nominally flat surfaces,” *Proceedings of the Royal Society of London. Series A, Mathematical and Physical Sciences*, vol. 295, no. 1442, pp. pp. 300–319, 1966.

[2] I. Nogueira, F. Robbe-Valloire, and R. Gras, "Experimental validations of elastic to plastic asperity-based models using normal indentations of rough surfaces," *Wear*, vol. 269, no. 11 12, pp. 709 – 718, 2010.

[3] S. Biwa, S. Hiraiwa, and E. Matsumoto, "Stiffness evaluation of contacting surfaces by bulk and interface waves," *Ultrasonics*, vol. 47, no. 1 4, pp. 123 – 129, 2007.

[4] G. Vermot des Roches, *Frequency and time simulation of squeal instabilities. Application to the design of industrial automotive brakes*. PhD thesis, École Centrale Paris, CIFRE SDTools, 2010.

[5] F. Moirot, *Etude de la stabilité d'un équilibre en présence de frottement de Coulomb*. PhD thesis, Ecole Polytechnique, 1998.

[6] X. Lorang, *Instabilité vibratoire des structures en contact frottant: Application au crissement des freins de TGV*. PhD thesis, Ecole Polytechnique, 2007.

[7] D. Vola, M. Raous, and J. A. C. Martins, "Friction and instability of steady sliding: squeal of a rubber/glass contact," *Int. J. Numer. Meth. Engng.*, vol. 46, pp. 1699–1720, 1999.

[8] G. D. Saxcé and Z. Q. Feng, "The bipotential method: A constructive approach to design the complete contact law with friction and improved numerical algorithms," *Mathematical and Computer Modelling*, vol. 28, no. 4-8, pp. 225–245, 1998. Recent Advances in Contact Mechanics.

[9] F. Jourdan, P. Alart, and M. Jean, "A gauss–siedel like algorithm to solve frictional contact problems," *Comput. Methods Appl. Mech. Engrg.*, vol. 155, pp. 31–47, 1998.

[10] O. Schenk and K. Gärtner, "Solving unsymmetric sparse systems of linear equations with pardiso," *Future Generation Computer Systems*, vol. 20, no. 3, pp. 475 – 487, 2004. Selected numerical algorithms.

[11] E. Balmes, J.-P. Bianchi, and G. Vermot des Roches, *Structural Dynamics Toolbox 6.4 (for use with MATLAB)*. SDTools, Paris, France, www.sdtools.com, October 2011.

[12] J.-P. Bianchi, E. Balmes, G. Vermot des Roches, and A. Bobillot, "Using modal damping for full model transient analysis," in *Proceedings of the International Conference on Advanced Acoustics and Vibration Engineering (ISMA)*, 2010.